U.P.B. Sci. Bull., Series D, Vol. 81, Iss. 2, 2019 ISSN 1454-2358

TEMPERATURE EFFECTS ON THE AXIAL STIFFNESS OF HYBRID METAL-COMPOSITE COUNTERSUNK BOLTED JOINTS

Calin-Dumitru COMAN[1], Dan Mihai CONSTANTINESCU[2]

A detailed 3D finite element model incorporating geometric, material and friction-based full contact nonlinearities is developed in this paper to numerically investigate the temperature effects on the stiffness of a hybrid metal-composite countersunk bolted joint. To validate the temperature effects on the joint stiffness, experiments were conducted using an Instron testing machine coupled to a temperature-controlled chamber. Experimental tests reveal that at negative temperatures the axial stiffness remains about the same and decreases with the increase of temperature. In numerical simulations the axial stiffness decreases gradually with the increase of temperature.

Keywords: temperature, hybrid joint, countersunk bolt, strain gauges, finite element method, stiffness.

1. Introduction

The aerospace industry became the most common application field for fiber-reinforced polymer matrix composites (PMCs) due to their lightweight properties [1]. These structural components are often assembled in conjunction with metal parts using mechanically fastened joints resulting in hybrid metal-composite joints which generate some challenging problems for mechanical engineers. Poorly designed hybrid joints are not only a source of failure but could lead to a reduction of the durability and reliability of the whole structure. Up to nowadays, the researchers studied the failure analysis of composite bolted joints using a method that combines continuum damage mechanics (CDM), [2], with finite element analysis (FEA). In the CDM case, the local damage onset appears at low values of the applied load and damage accumulation is developed with increasing load according to damage propagation laws, which makes the method accurate and able to predict various failure modes. The major disadvantage of the CDM models is the huge amount of test data required for model calibrations. The progressive damage analysis (PDA) of composite materials, which is based on the stress-strain failure

---

[1] PhD student and Eng., Dept. of Structures and Materials, National Institute of Aerospace Research INCAS Bucharest, Romania, email: coman.calin@incas.ro

[2] Prof., Dept. of Strength of Materials, University POLITEHNICA of Bucharest, Romania, e-mail: dan.constantinescu@upb.ro

criterion [3], showed that the material orthotropic properties reduction due to damage initiation is essential for the stress field analysis [4-7].

Models containing continuous degradation rules started to appear in the literature [8, 9], as to improve the numeric algorithm convergence and to obtain a smoother load-displacement curve. One major lack of these models is that they focused only on few types of failure modes and were not considering the various joint failure modes. The composite progressive damage behavior is a complex nonlinear phenomenon and in conjunction with geometric and contact nonlinearities can lead to loss of convergence in the finite element method (FEM) analysis, mostly in implicit numerical algorithms which imply that many efforts are paid for obtaining a valid solution towards the prediction of the ultimate global structure failure.

The composite materials can withstand an increased temperature up to 300 ^{0}C, having good properties as: high pressure resistance, high thermal conductivity, high thermal shock resistance and low depression [10]. The difficulties arising from composite materials usage on structural failure problems are that these materials have anisotropic mechanical properties, brittle behavior and low inter-laminar strength [11]. Another issue is the damage in composite materials variation with the temperature as it is described in [12-15]. Airplane structures can be exposed to rush environment conditions which can imply the joints strength loss because of environmental ageing and temperature variations, these topics being studied in the research community [16-21].

In this study it is described and developed a progressive damage analysis using an adequate material model for composite adherend that can predict the thermal effects on the structural behavior and the failure of the hybrid metal-composite bolted joints by taking into account all the nonlinearities phenomena involved in the load transfer through the joint as geometric nonlinearity which imply: large deformations, friction based full nonlinear contact and material nonlinearities due to the lamina shear deformations. The experimental and numerical results fit together quite accurately capturing also the influence of temperature on the axial stiffness and failure load of the hybrid metal-composite bolted joints.

2. Experimental problem description

Single-lap joints (SLJs) with countersunk bolts were manufactured using both metal and composite materials for the adherends. The geometry of the joint model is presented in Fig. 1. The joint design was chosen in accordance with ASTM D 5961 standard [22] to induce bearing failure. The dimensions of each adherend are the same, as follows: 150 mm length and 50 mm width, but the thicknesses are different, the metal adherend has 4 mm thickness and the composite laminated adherend has 2 mm; a similar geometry was used before in [23]. Countersunk head stainless steel bolts with nominal diameter of 4 mm and a 0.5 Nm torque level were used in dry conditions at 23 °C. The composite adherend was manufactured from carbon-epoxy pre-pregs with 32% fiber volume fraction. The stacking sequence of the composite adherend is represented by [0/90/0/90/0/90] using 0.33 mm thickness unidirectional lamina, with the elastic properties presented in Table 1. The metal adherend was manufactured from aluminum alloy AA 7075T6 and the bolts, nuts and washers were fabricated from stainless steel A2-70 with the elastic properties presented in Table 2.

Table 1

Composite material properties

Property	Carbon fibers [27]	Epoxy matrix [28]	Lamina EXP
Longitudinal modulus E_{11} (MPa)	230000	3200	34433
Transversal modulus E_{22} (MPa)	6000	3200	3610
Through-thickness modulus, E_{33} (MPa)	-	3200	3610
Shear modulus G_{12} (MPa)	18000	1300	2421
Shear modulus G_{13} (MPa)	-	1300	2421
Shear modulus G_{23} (MPa)	-	1300	1561
Poisson coefficient ν_{12}	0.36	0.35	0.36
Poisson coefficient ν_{23}	-	0.35	0.45
Poisson coefficient ν_{13}	-	0.35	0.35
Longitudinal CTE α_{11} (10^{-6}/°C)	-0.04	4	2
Transversal CTE α_{22} (10^{-6}/°C)	-	-	44
Through-thickness CTE α_{33} (10^{-6}/°C)	-	-	44
Longitudinal tensile strength $\sigma_{11,\,max}^{T}$, (MPa)	3530	86	253
Longitudinal compression strength $\sigma_{11,\,max}^{C}$, (MPa)	-	-	230
Transversal compression strength $\sigma_{22,\,max}^{C}$, (MPa)	-	-	74
In plane shear strength τ_{12}^{max}, (MPa)	-	-	25
Out plane shear strength τ_{23}^{max}, (MPa)	-	-	37
Out plane shear strength τ_{13}^{max}, (MPa)	-	-	37

Regarding the clamping of the joint in the testing machine, the boundary conditions imposed on the FE model are presented in Fig.1. The displacements u, v and w are defined in x, y and z directions. The boundary conditions represent clamping the nodes on top and bottom surfaces at the leftmost end of the metal adherend and blocking the translations on y and z directions (v and w) at the rightmost end of the composite adherend. For simulating the quasi-static loading condition of the testing machine, a prescribed displacement, on x direction (u) is used for the nodes from both surfaces of the composite adherend at the rightmost end. The dimensions of the joint geometry are designed in such a way that allow the bearing failure in the laminated composite adherend, as presented also in [23], and are explained in Fig. 2.

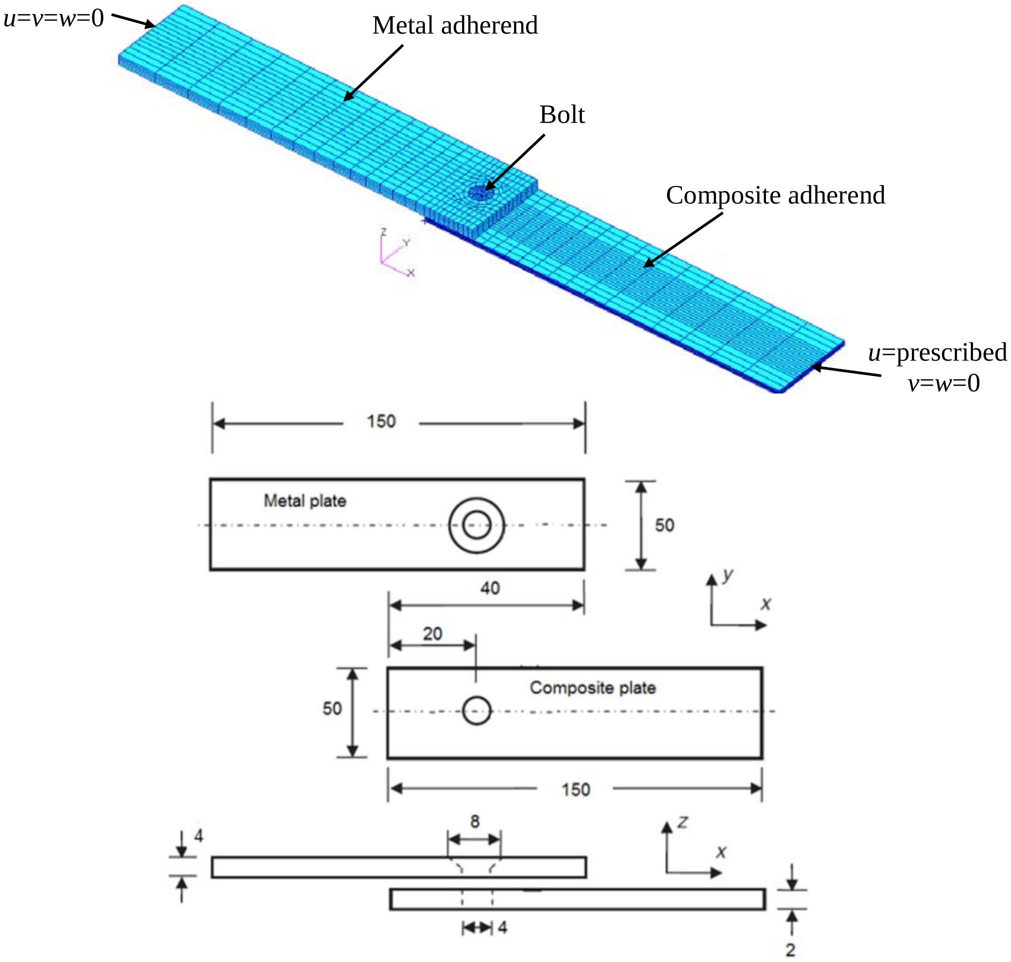

Fig. 1. Countersunk joint geometry and boundary conditions, all dimensions in mm, [23]

$$\frac{b}{D} > 4$$

$$\frac{e}{D} > 3$$

$$1.5 \leq \frac{D}{t} \leq 3.0$$

$$0 \leq \frac{h}{t} \leq 0.7$$

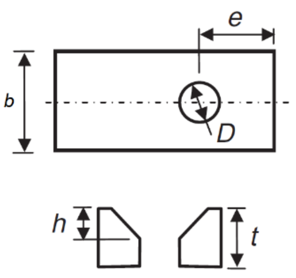

Fig. 2. Specimen dimensions for bearing failure mode, [23]

The mechanical properties of the materials used are presented in Tables 1 and 2, where the lamina orthotropic directions (1, 2, 3) are the same with global coordinate axes (x, y, z) shown in Fig. 1. The lamina elastic properties presented in

Table 1 were obtained using ASTM [24-26] standard tests on the unidirectional laminated specimens. Regarding the thermal expansion coefficient of the composite adherend, it has been used a micro-analysis method to calculate this coefficient at lamina level using the thermal coefficients of the fibers and matrix. According to [27] and [28] we have α_{fiber}= - 0.41·10^{-6}/ °C, α_{matrix}= 40 ·10^{-6}/ °C. Using these values and equation (1) it can be obtained, [29]:

$$\alpha_{11}=\frac{E_{fiber}\cdot V_{fiber}\cdot \alpha_{fiber}+E_{matrix}\cdot (1-V_{fiber})\cdot \alpha_{matrix}}{E_{11}}=2\cdot 10^{-6}/^{\circ}\mathrm{C} \qquad (1)$$

and $\alpha_{22}=\alpha_{33}=44\cdot 10^{-6}/^{\circ}\mathrm{C}$.

Table 2

Isotropic material properties [30]

Property	AA 7075T6	A2-70
Elastic modulus, *E* (MPa)	71016	206000
Shear modulus, *G* (MPa)	26890	75842
Poisson coefficient, ν	0.33	0.36
Thermal coefficient, CTE α (10^{-6}/°C)	24	18

After joint mounting, the specimen was gripped in the 30 kN Instron 3367 testing machine, connected to a temperature-controlled chamber, Fig. 3. The chamber is Instron SFL 3119-400, temperature controlled (-70/+250 °C) with liquid CO_2 as freezing agent. The bearing tests were conducted in accordance with ASTM 5961 standard, [22], and the specimens were loaded with a displacement rate of 0.3 mm/min until ultimate failure for the temperature values, T_1= +50 °C, T_2= -50 °C, T_3= +70 °C and T_4= -70 °C.

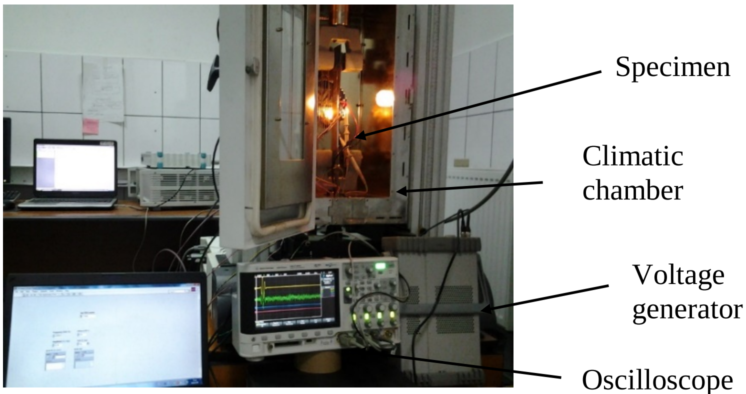

Fig. 3. Experimental workbench with temperature-controlled ch

3. Numerical model description

A tridimensional (3D) FEM, using linear brick elements with eight nodes was developed in the commercial software MSC Patran for the joint geometry model, as shown in Fig. 4. Each separate part was modeled: metal and composite adherends, the washer and a combined bolt-nut part. The adherends were modeled with increased radial mesh density around the hole, where high strain gradients exist. As to avoid rigid body motions, light springs were attached to the components not fully constrained, such as the bolt, washer and laminated adherend. For simulating the bolt pre-load due to the applied torque level, a 330 N axial force was applied in the bolt shank using Bolt Preload Module in Patran.

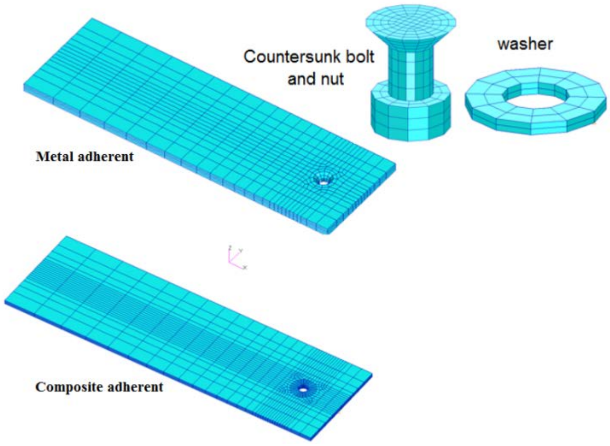

Fig. 4. 3D finite element model.

The laminated adherend is modelled with continuum solid-shell special elements available in MSC Nastran 2012. These special solid elements have bending properties like shells and one integrating point per element is considered. The finite element model has six elements across the laminate thickness, with one solid-shell element per each ply, thus, stress in each ply can be determined and the correct bending-twisting coupling is obtained. The dimension for each part of the FE model is described in Table 3. The FE model was refined near the hole, due to the stress concentrators. Thus, the minimum element length is 0.33 mm around the hole. The minimum element length is increasing from hole towards the clamped ends of the adherends. In the 3D model, the contact with clearance between the bolt and surface of the hole is realized as the follows. The method requires the definition of the bodies that can come into contact.

Table 3

FEM description

Part	Elements	Nodes
Composite adherend	3568	3284
Metal adherend	2413	2318
Bolt	862	824
Washer	394	357
All	7237	6783

The contact bodies may be the whole physical bodies (laminated adherends, bolt, washer), but it has been shown in [31] that it is more efficient to consider sets of elements of these physical bodies, as shown in Fig. 5, because the number of checks for contact between bodies at each iteration of the solution is reduced.

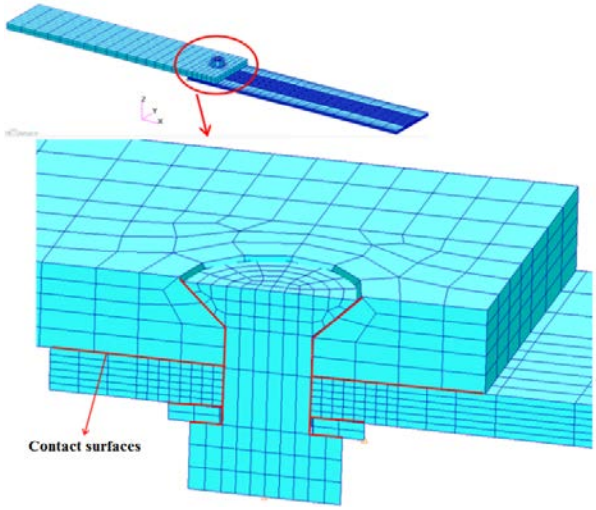

Fig. 5. Contact elements in 3D model, contact surfaces marked with red colour.

Another step in defining nonlinear contact phenomena is the choice between the analytical contact and the discreet contact, which will be briefly described below. When a node on a solid reaches the contact segment on the other contact body, the node is constraint on this segment with respect to the normal of this segment. In the case of discrete contact for normal detection, the linear representation with the finite elements of the contact surface is used, which leads to the calculation of the normal of each element. If the surface is not planar, then when a node touches the contact segment, it is blocked between two different normal elements due to the discontinuity of the normal elements, because it is shifted and constrained on the contact segment. This impediment has an adverse effect on the quality of the results as observed by McCarthy et al. [31] in their work on composite bolted joints.

In the case of analytical contact, a smooth Coons surface is constructed through the nodes of the solid contact segment, and then this analytical surface is used to calculate the normal of the contact surface between the two solids, thus solving the problem of node blocking due to the discontinuity of the surface normal between the bodies. This method leads to a better representation of the geometry of the joint, especially its deformation and the accuracy of the numerical results is far superior to the technique of discrete contact, [31].

4. Temperature effects on joint stiffness

4.1 Model validation

In this section, the results from the tests are compared with the ones of the three-dimensional finite element model described in the previous chapter. Strains at the selected points on the surface of the laminated adherend are used to check the accuracy of the finite element model. The joints were strain gauged and loaded in tension to a level that prevents any damage of the composite adherend (1.2 kN load) at T_1 = +50 °C. Fig. 6 presents the locations of the 3 mm length strain gauges, type 1-Ly16-3/350, with 350 Ω electrical resistance, fabricated by HBM; gauges 1, 3, and 4 are aligned with the loading direction and located on the bottom surface of the laminate adherend, except the gauge number 2 which is located in the shear plane on the top surface of the composite adherend.

The numerically calculated and experimentally measured strains are given in Table 4 and Fig. 7. In Fig. 7 EXP curves denote experimental strains and FEM the numerical ones. From the Table 4 it is clearly seen that strain gauges 1 and 2 indicate a joint bending even though the loading is a tensile one. The strain readings for gauges 3 and 4 are quite different, thus indicating a misalignment (twisting) effect of the joint along the longitudinal axis, which is the loading *x* axis. As a conclusion, from Table 4, it can be considered that the model has predicted the linear behavior of the joint quite satisfactory and can be further used in the temperature parametric study for the linear response of the hybrid metal-composite joint.

Table 4

Experimental and numerical strain readings, 1.2 kN applied load

Gauge number	Experimental strain (μm/m)	Numerical strain (μm/m)
1	776	810
2	-1300	-1252
3	757	689
4	679	615

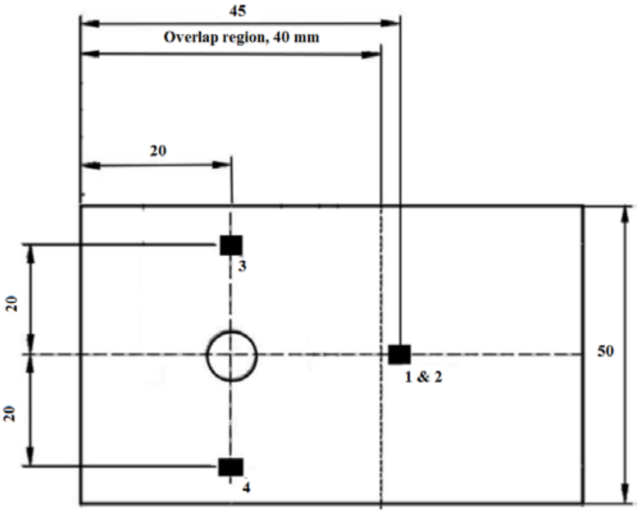

Fig. 6. Strain gauge locations, all dimensions in mm.

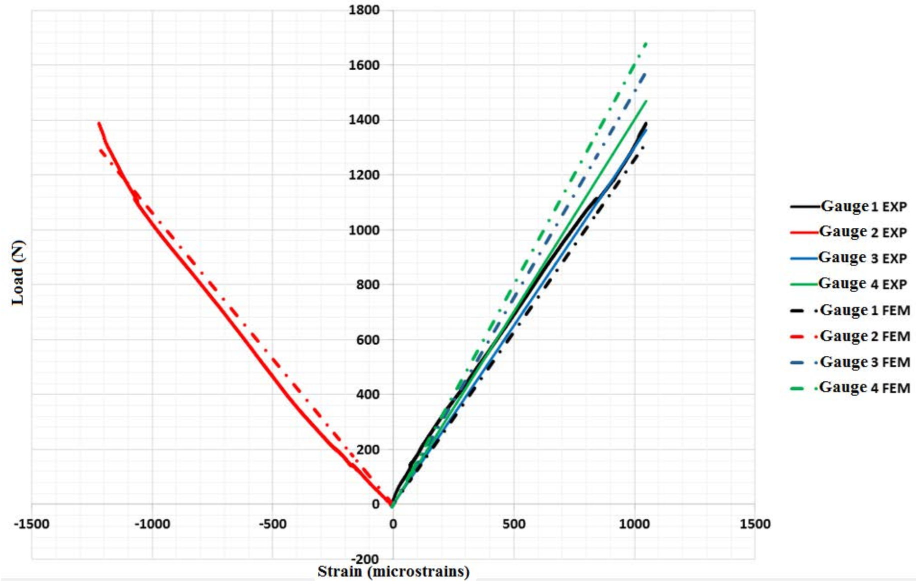

Fig. 7. Experimental and numerical surface strains.

4.2 Joint stiffness

The effects of temperature on the joint axial stiffness are presented in this subchapter. From the experimental results, it was observed in Fig. 8 that the load-displacement curves are approximately linear, for applied load between 0.2 - 1 kN in the experiment and 0.1-1.5 kN in the simulation for the temperature T_1 = +50 ^{0}C, but in between 0.1-3.3 kN in experimental testing and 0.2-3.5 kN in FEA for the temperature T_2 = - 50 ^{0}C; so the stiffness of the joint is determined for these load ranges. The joint load was obtained directly from testing machine and the displacement was measured with an optical extensometer (Instron Advanced Video Extensometer). The load-displacement curves for the four temperature values are presented in Fig. 8.

The first nonlinear segments on the experimental curves from Fig. 8 are explained by the friction between the adherends. For the low level of the applied load, the forces are transmitted through friction between the adherends without relative movement, so the shank of the bolt don’t bear the hole surface due to the initial clearance in the joint. The joint under investigation has a close tolerance clearance equal to 48 µm according to f7H10, [32], standard fit tolerances.

As long as $F > \mu P$, where F is the applied load, μ=0.235 is chosen to be the frictional coefficient between aluminum AA 7075 and CFRP adherends, as Schon [33] measured experimentally, and P = 330 N is the adherends clamping force due to bolt torque; the friction is overcome and the bolt shank moves toward the hole surface, reducing the joint clearance.

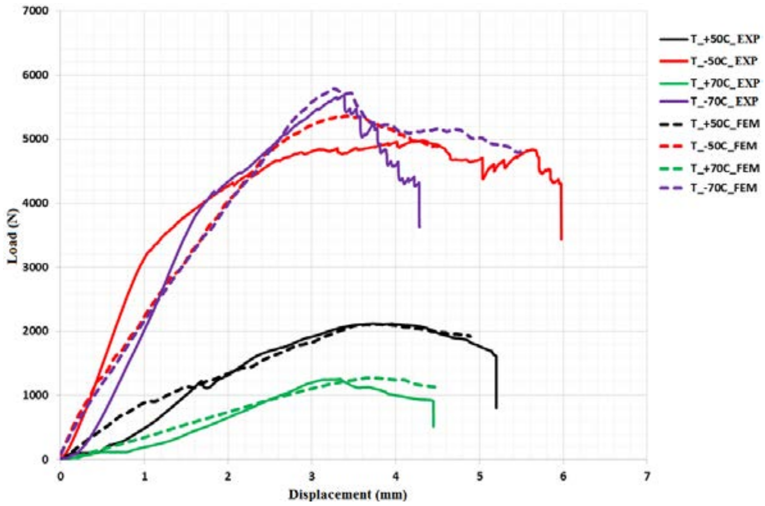

Fig. 8. Load-displacements characteristic curves.

Once the bolt fully contacts the hole surface, the joint is elastically deformed, the joint axial stiffness is developed and can be determined. The experimental and numerical joint axial stiffness, calculated as the slope of the approximately linear portions of the load-displacement curves in the load ranges mentioned above, are presented in Table 5. From this, it can be observed that the temperature increase reduces the stiffness of the hybrid metal-composite joint both in the experiment and simulation, because the matrix has plastic strains under high temperature and due to the low volume ratio of carbon within the composite material (32 %).

Table 5

Thermal effects on axial stiffness

Stiffness (kN/mm)		Temperature (^{0}C)
Experiment	Simulation	
2.86	1.94	-70
3.49	1.83	-50
1.04	1.66	+50
0.53	0.38	+70

5. Conclusions

In this paper, the thermal effects on the stiffness and damage initiation for single-lap, single-bolt, hybrid metal-composite joints are investigated using both experimental strain gauge measurements and a finite element analysis. The joint geometry dimensions are designed according to ASTM [22] standard for bearing failure. The countersunk bolt was chosen as it determines a complex tridimensional state of stress around the hole and thus a relevant mode of failure in the composite adherend of the joint.

The simulation results were in good agreement with the experiments in terms of load-displacement behavior, surface strains, joint stiffness, thus denoting that the 3D FEM model including full nonlinearities for explicit solver are quite accurate and can predict the metal-composite joint's mechanical behavior on both linear-elastic and nonlinear elastic ranges.

When analyzing the temperature effects on the joint stiffness, an evident decrease of the stiffness of the joint in the axial direction is produced as temperature increases. However, experimental strain measurements give an approximately constant stiffness at negative temperatures, being highest at -50 ^{0}C, and then a decrease when temperature rises, as numerical simulations show a decrease of the stiffness as temperature increases from -70 ^{0}C to +70 ^{0}C.

REFERENCES

[1] *Y. Xiao, T. Ishikawa*, Bearing strength and failure behavior of bolted composite joints, part II: modeling and simulation, Composites Science and Technology, **vol. 65**, no. 7-8, 2005, pp. 1032–1043.

[2] *J.L. Chaboche*, Continuum damage mechanics: part II – damage growth, crack initiation and crack Growth, Journal of Applied Mechanics, **vol. 55**, no. 1, 1988, pp. 59–72.

[3] *F.K. Chang, K.Y. Chang*, Post-failure analysis of bolted composite joints in tension or shear-out mode failure, Journal of Composite Materials, **vol. 21**, no. 9, 1987, pp. 809–33.

[4] *L.B. Lessard, M.M. Shokrieh*, Two-dimensional modeling of composite pinned-joint failure, Journal of Composite Materials, **vol. 29**, no. 5, 1995, pp. 671–97.

[5] *C.L. Hung, F.K. Chang*, Bearing failure of bolted composite joints. Part II: model and verification, Journal of Composite Materials, **vol. 30**, no. 12, 1996, pp. 1359–400.

[6] *S.J. Kim, J.S. Hwang, J.H. Kim*, Progressive failure analysis of pin-loaded laminated composites using penalty finite element method, AIAA Journal, **vol. 36**, no. 1, 1998, pp. 75–80.

[7] *P.P. Camanho, F.L. Matthews*, A progressive damage model for mechanically fastened joints in composite laminates, Journal of Composite Materials, **vol. 33**, no. 24, 1999, pp. 2248–80.

[8] *A.K. Zerbst, G. Kuhlmann, C. Steenbock*, Progressive damage analysis of composite bolted joints with liquid shim layers using constant and continuous degradation models, Composite Structures, **vol. 92**, no. 2, 2010, pp. 189–200.

[9] *G. Kolks, KI. Tserpes*, Efficient progressive damage modeling of hybrid composite/titanium bolted joints. Composites A: Applied Science and Manufacturing, **vol. 56**, no.1, 2014, pp. 51–63.

[10] *B. Egan, M.A. McCarthy, R.M. Frizzell, P.J. Gray, C.T. McCarthy*, Modelling bearing failure in countersunk composite joints under quasi-static loading using 3D explicit finite element analysis, Composite Structures, **vol. 108**, 2014, pp. 963–977.

[11] *A. Olmedo, C. Santiuste, E. Barbero*, An analytical model for the secondary bending prediction in single-lap composite bolted-joints, Composite Structures, **vol. 111**, 2014, pp. 354–361.

[12] *H. da Costa Mattos, J. Reis, L. Paim, M. da Silva, F. Amorim, V. Perrut*, Analysis of a glass fibre reinforced polyurethane composite repair system for corroded pipelines at elevated temperatures, Composite Structures, **vol. 114**, 2014, pp. 117–23.

[13] *J. Reis, J. Coelho, A. Monteiro, H. da Costa Mattos*, Tensile behavior of glass/epoxy laminates at varying strain rates and temperatures, Composites Part B: Engineering, **vol. 43**, no. 4, 2012, pp. 2041–2046.

[14] *J. Reis, J. Coelho, H. da Costa Mattos*, A continuum damage model for glass/epoxy laminates in tension, Composites Part B: Engineering, **vol. 52**, 2013, pp. 114–9.

[15] *J. Reis, F. Amorim, A. da Silva, H. da Costa Mattos*, Influence of temperature on the behavior of DGEBA (bisphenol A diglycidyl ether) epoxy adhesive, International Journal of Adhesion and Adhesives, **vol. 58**, 2015, pp. 88–92.

[16] *J. Zhengwen, W. Shui, W. Zhishen*. Calculation of energy release rate for adhesive composite/metal joints under mode-I loading considering effect of the non-uniformity, Composites Part B: Engineering, **vol. 95**, 2016, pp. 374–85.

[17] *M. Heshmati, R. Haghani, M. Al-Emrani*, Durability of bonded FRP-to-steel joints: effects of moisture, de-icing salt solution, temperature and FRP type, Composites Part B: Engineering, **vol. 119**, 2017, pp. 153–167.

[18] *T. Kleffel, D. Drummer*, Investigating the suitability of roughness parameters to assess the bond strength of polymer-metal hybrid structures with mechanical adhesion, Composites Part B: Engineering, **vol. 117**, 2017, pp. 20–25.

[19] *A. Agarwal, S. Foster, E. Hamed*, Wet thermo-mechanical behavior of steel–CFRP joints – an experimental study, Composites Part B: Engineering, **vol. 83**, 2015, pp. 284–296.

[20] *A. Agarwal, S. Foster, E. Hamed, A. Vrcelj*, Testing of steel-CFRP adhesive joints under freeze-thaw cycling, Conf. Mech. Struct. Mater. ACMSM 2012, pp. 801–6.

[21] *M. Heshmati, R. Haghani, M. Al-Emrani*, Effects of moisture on the long-term performance of adhesively bonded FRP/steel joints used in bridges, Composites Part B: Engineering, **vol. 92** 2016, pp. 1–16.

[22] ***ASTM D 5961, Standard test method for bearing response of polymer matrix composite laminates, ASTM International, USA, 2007.

[23] *M. Chishti, H. Wang, S. Thomson, C. Orifici*, Experimental investigation of damage progression and strength of countersunk composite joints, Composite Structures **vol. 94**, no. 3, 2012, pp. 865–873.

[24] ***ASTM D 3039, Standard Test Method for Tensile Properties of Polymer Matrix Composite Materials, ASTM International, USA, 2002.

[25] *** ASTM D 3410, Standard Test Method for Compressive Properties of Polymer Matrix Composite Materials, ASTM International, 2007.

[26] *** ASTM D 5379, Standard Test Method for Shear Propeties of Composite Materials by the V-Notched Beam Method, ASTM International, 2008.

[27] ***Torayca T300, Technical Data Sheet No. CFA-001, Toray Carbon Fibers America Inc.

[28] ***Derakane Momentum 411-350 Epoxy Venyl Ester Resin, Technical Data Sheet No. 1701 V3 F2, Ashland Inc.

[29] ***ECSS-E-HB-32-20 Part 2A, Structural materials handbook - Part 2: Design calculation methods and general design aspects, ESA ESTEC, 2011.

[30] ***Metallic Materials Properties development and Standardization (MMPDS-05), Federal Aviation Administration, USA, 2010.

[31] *M. A. McCarthy, C. T. McCarthy, V. P. Lawlor, W. F. Stanley*, Three-dimensional finite element analysis of single-bolt, single-lap composite bolted joints: part I - model development and validation, Composite Structures, **vol. 71**, no. 2, 2005, pp.140–158.

[32] *** ISO 286-2, Geometrical product specifications (GPS) – ISO code system for tolerances on linear sizes- Part 2: Tables of standard tolerance classes and limit deviations for holes and shafts, International Organization for Standardization, 2010.

[33] *J. Schon*, Coefficient of friction for aluminum in contact with a carbon fiber epoxy composite. Tribology International, **vol. 37**, no. 5, 2004, pp. 395–404.